materials

MDPI

Article

Luminescent Properties and Optical Temperature Sensing Performance of $CaTa_2O_6$:Pr^{3+} Phosphors Under Blue-Light Excitation

Quan Jiang [1,2], Jian Ruan [1,2,*], Chen Tian [2,3,*], Zijing Zhu [1,2], Shuang Zhang [1,2] and Chao Liu [1,2]

[1] State Key Laboratory of Advanced Glass Materials, Wuhan University of Technology, Wuhan 430070, China; quanjiang_0382@whut.edu.cn (Q.J.); zijing@whut.edu.cn (Z.Z.); shuangzhang_22@whut.edu.cn (S.Z.); hite@whut.edu.cn (C.L.)
[2] Research Center for Silicate Materials Engineering, Wuhan University of Technology, Wuhan 430070, China
[3] State Key Laboratory of Silicate Materials for Architectures, Wuhan University of Technology, Wuhan 430070, China
* Correspondence: jian_ruan@whut.edu.cn (J.R.); tianchen@whut.edu.cn (C.T.)

Highlights

- The concentration-dependent luminescence of $CaTa_2O_6$:Pr^{3+} phosphors under blue-light excitation is presented.
- Emission enhancement via Pr^{3+}/Zr^{4+} or Pr^{3+}/Sn^{4+} co-doping is found.
- The temperature-dependent luminescence of the $CaTa_2O_6$:Pr^{3+}, Sn^{4+} phosphor and a PiG based on it are studied.
- The FIR mode based on $^3P_1 \rightarrow {}^3H_5/{}^3P_0 \rightarrow {}^3F_2$ of Pr^{3+} is found to be promising for luminescence thermometry.

Abstract

Pr^{3+}-activated phosphors are promising for non-contact optical thermometry under blue-light excitation. In tantalate hosts, Pr^{3+}-Ta^{5+} intervalence charge transfer (IVCT) states may introduce thermally activated nonradiative pathways involving the $^3P_0$ and $^1D_2$ levels, thus affecting their thermal quenching behavior and thermometric performance. However, the concentration- and temperature-dependent luminescence of $CaTa_2O_6$:Pr^{3+} remains unexplored. In this study, $CaTa_2O_6$:Pr^{3+} phosphors were synthesized via the solid-state reaction method, and a phosphor-in-glass (PiG) composite was fabricated by co-sintering the mixture of the phosphor and the precursor glass (PG) powder. The structural characteristics and the luminescence properties of $CaTa_2O_6$:Pr^{3+} phosphors under 450 nm excitation were investigated. The IVCT band was confirmed in the excitation spectrum. Optimal Pr^{3+} concentrations were 2 mol% for ^3P_J and 0.7 mol% for $^1D_2$ emissions. With Pr^{3+}/Zr^{4+} or Pr^{3+}/Sn^{4+} co-doping, the emission intensity was enhanced by 1.34 and 1.31 times, respectively. The PiG exhibited similar spectral profiles. An FIR mode based on $^3P_1 \rightarrow {}^3H_5/{}^3P_0 \rightarrow {}^3F_2$ transitions achieved maximum relative sensitivities of 1.09% K^{-1} for the phosphor and 1.18% K^{-1} for the PiG at 298 K. These findings suggest that $CaTa_2O_6$:Pr^{3+}-based materials are potential candidates for luminescence thermometry.

Keywords: Pr^{3+}; $CaTa_2O_6$ phosphor; optical temperature sensing; fluorescence intensity ratio; IVCT state; phosphor-in-glass

Check for updates

Academic Editor: Dirk Poelman

Received: 20 April 2026
Revised: 18 May 2026
Accepted: 20 May 2026
Published: 1 June 2026

Copyright: © 2026 by the authors. Licensee MDPI, Basel, Switzerland. This article is an open access article distributed under the terms and conditions of the Creative Commons Attribution (CC BY) license.

1. Introduction

Pr^{3+}-activated inorganic phosphors are promising for optical sensing because of their abundant energy levels in the $4f^2$ electronic configuration and excellent luminescence properties [1,2]. Luminescence thermometry has attracted considerable attention because of its non-contact nature, rapid response, and strong resistance to electromagnetic interference [3,4]. The fluorescence intensity ratio (FIR) technique is particularly attractive because of its self-referencing feature, which minimizes the effects of excitation fluctuations and improves measurement reliability [5]. In particular, the thermally coupled $^3P_1/^3P_0$ levels of Pr^{3+} ions enable a typical Boltzmann-type temperature response. Moreover, in oxide hosts containing d^0 cations, such as Ti^{4+}, Nb^{5+} or Ta^{5+}, the luminescence of Pr^{3+} is frequently affected by intervalence charge transfer (IVCT) states. It provides an efficient nonradiative channel for electron relaxing from excited state $^3P_0$ to excited state $^1D_2$ due to its strongly temperature-dependent behavior, so that the IVCT process can significantly improve optical thermometric performance [6–9].

Recently, $CaTa_2O_6$ has been proven to be a promising host for rare-earth ion activators because of its high stability [10–13]. The presence of Ta^{5+} provides favorable conditions for the formation of Pr^{3+}-Ta^{5+}-related IVCT states. $CaTa_2O_6$:Pr^{3+} has been reported to exhibit unusual greenish blue emission with a pronounced contribution from the $^3P_0$ level, suggesting that the IVCT state in this host is not sufficiently effective to fully quench the $^3P_0$ emission. In addition, multiple electron trapping centers have been identified in $CaTa_2O_6$:Pr^{3+}, indicating that defect-assisted processes also contribute to its luminescence and thermal relaxation behavior [14]. Therefore, the luminescence of Pr^{3+} in $CaTa_2O_6$ is governed by the combined effects of intrinsic 4f-4f transitions, IVCT-assisted relaxation, and defect-related nonradiative processes, resulting in temperature-dependent behavior distinct from that of conventional thermally coupled-level systems [15,16]. Nevertheless, the concentration- and temperature-dependent luminescence of $CaTa_2O_6$:Pr^{3+} under blue-light excitation remains unexplored, but this is significant in understanding the thermal sensitivity of its luminescence and assessing its potential for optical thermometry.

Moreover, Pr^{3+}-activated phosphors could benefit efficient excitation via commercially available blue-light sources in the 440–470 nm range [17]. This makes them favorable for compact and low-cost non-contact thermometric devices. Furthermore, a phosphor-in-glass (PiG) composite approach would allow it to be used as a fiber-optic probe material. Because the inorganic glass matrix offers superior thermal stability, moisture resistance, and long-time durability compared with conventional silicone or resin packing, the PiG material would be promising for fiber-integrated optical thermometry [18].

Therefore, in this study, the photoluminescence properties of $CaTa_2O_6$:Pr^{3+} phosphors under 450 nm excitation are reported. Their phase structures and morphologies were examined. The Pr^{3+} concentration-dependent luminescence and the effect of charge compensation by Sn^{4+} and Zr^{4+} co-doping were investigated. Furthermore, a PiG sample combining the $CaTa_2O_6$:0.02Pr, 0.02Sn phosphor and the $30ZnO$-$30Bi_2O_3$-$40B_2O_3$ glass was fabricated. The temperature-dependent luminescence and optical thermometric performance of the phosphor and the PiG based on it were evaluated. The results are expected to provide useful guidance for the development of Pr^{3+}-activated tantalate luminescent thermometric materials and related PiG devices.

2. Materials and Methods

The conventional high-temperature solid-state reaction method was used for preparing $Ca_{1-x}Ta_2O_6$:xPr^{3+} (x = 0.005–0.05) and charge-compensated $Ca_{0.98}Ta_{1.98}O_6$:$0.02Pr^{3+}$, $0.02M^{4+}$ (M = Zr and Sn) phosphors. Stoichiometric amounts of $CaCO_3$ (99.9%), Ta_2O_5 (99.5%), Pr_6O_{11} (99.0%), SnO (99.0%), and ZrO_2 (99.0%) were thoroughly mixed and ground

and then calcined in alumina crucibles at 800 °C for 1 h and 1200 °C for 6 h, followed by cooling to room temperature. Then, 3 wt% H_3BO_3 (99.0%) was added as a flux for sintering. The obtained products were crushed and reground into powders. For simplicity, all $CaTa_2O_6$-based phosphors are denoted as CTO:*x*Pr, CTO:0.02Pr, 0.02Sn, or CTO:0.02Pr, 0.02Zr hereafter. Low-melting glass powders were prepared via the traditional melt-quenching route. The nominal chemical composition of the precursor glass (PG) is 30ZnO-30Bi_2O_3-40B_2O_3 (in mol%), denoted as 30Zn30Bi40B. The raw materials of ZnO (99.0%), Bi_2O_3 (99.0%), and H_3BO_3 (99.0%) were mixed and melted at 800 °C for 1 h to obtain homogeneous glass melts. The glass was formed in a stainless-steel mold and then cooled to room temperature. Then, it was crushed and ground into powders. The PiG samples were fabricated from the mixture of the $CaTa_2O_6$:0.02Pr, 0.02Sn phosphor and the 30Zn30Bi40B glass powder with a weight ratio of 1:9. After being thoroughly ground, the phosphor–glass powder mixture was pressed into a disk-shaped pellet and then co-sintered in a muffle furnace at 480 °C for 1 h. After cooling to room temperature, the PiG samples were obtained.

The phase compositions of both the phosphor samples and the PiG sample were characterized by X-ray diffraction (XRD, Bruker D8 Advance, Cu Kα radiation) in the 2θ range of 10–80° with a step size of 0.02°, and the phases were identified by comparison with standard PDF cards. The microstructure and elemental distribution were investigated by field-emission scanning electron microscopy (FE-SEM, Zeiss Ultra Plus) coupled with energy-dispersive X-ray spectroscopy (EDS, X-Max50). For the PiG sample, EDS analysis was performed to distinguish the glass and crystalline phases and to evaluate their interfacial features. The thermal behavior of the PG was studied by differential scanning calorimetry (DSC, STA449F3) under flowing Ar at a heating rate of 10 °C min^{-1}. The diffuse reflectance spectra of the phosphors and transmittance spectra of the PG were measured with a UV–vis–NIR spectrophotometer (Lambda 750 S). Photoluminescence excitation and emission spectra were recorded on a PTI QM/TM/NIR spectrofluorometer using an MDL-III-450 laser as the excitation source, with a step size of 1 nm and an integration time of 0.1 s. Temperature-dependent luminescence measurements were carried out on the same system fitted with a TAP-02 high-temperature fluorescence controller over 298–573 K, using a temperature interval of 25 K and a holding time of 5 min at each temperature.

3. Results and Discussion

3.1. $CaTa_2O_6:Pr^{3+}$ Phosphors

3.1.1. Phase Structure and Morphology

The XRD patterns of the $CaTa_2O_6:Pr^{3+}$ phosphors are given in Figure 1a. It can be seen that all diffraction peaks could be well indexed to the standard pattern of β-$CaTa_2O_6$. This suggests that the β-$CaTa_2O_6$ phase was successfully obtained in CTO:*x*Pr (x = 0.005–0.05), CTO:0.02Pr, 0.02Sn, and CTO:0.02Pr, 0.02Zr samples. No obvious peaks from secondary phases were observed. These results indicate that the CTO host exhibits good structural tolerance toward Pr^{3+} doping and charge compensation.

Figure 1b illustrates the crystal structure of β-$CaTa_2O_6$ (space group Pnma, No. 62), in which Ca^{2+} occupies an eight-coordinated site and Ta^{5+} occupies a six-coordinated site. Based on the Shannon ionic radii [19], Pr^{3+} (1.13 Å, CN = 8) is expected to substitute Ca^{2+} (1.12 Å, CN = 8) owing to their comparable sizes. In contrast, Zr^{4+} (0.72 Å, CN = 6) and Sn^{4+} (0.69 Å, CN = 6) exhibit ionic radii similar to that of Ta^{5+} (0.64 Å, CN = 6) under six-fold coordination, suggesting the preferential occupancy of the Ta sites. Such site-selective doping helps to preserve the structural stability of the β-$CaTa_2O_6$ host.

As shown in Figure 1c, irregular particles with an average size of 1.8 μm were observed in the CTO:0.02Pr,0.02Sn sample. Slight particle agglomeration was also found, which was

likely caused by particle coalescence and grain growth during high-temperature sintering [20]. It suggests that the phosphor should be suitable for PiG fabrication. Moreover, the presence of Ca, Ta, O, Pr, and Sn was confirmed by EDS analysis. As given in Figure 1d, the atomic ratio of Ca to Ta is close to 1:2, in good agreement with the stoichiometry of $CaTa_2O_6$, while the slightly reduced Ca content can be ascribed to the partial substitution of Ca by Pr and Sn.

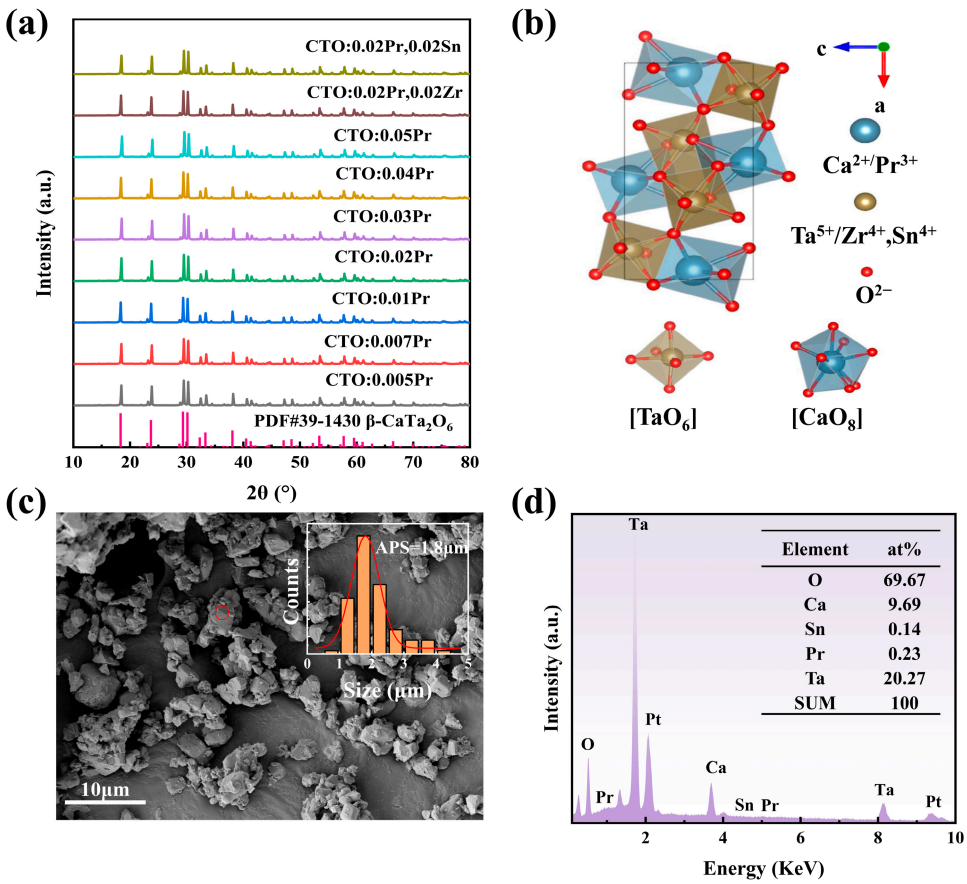


Figure 1. (**a**) XRD patterns of CTO: Pr^{3+} phosphors with various Pr^{3+} doping concentrations and different charge compensators; (**b**) crystal structure of β-$CaTa_2O_6$; (**c**) SEM image of the CTO:0.02Pr, 0.02Sn phosphor, the red circle marks the position selected for EDS analysis, and the inset shows the particle size distribution; (**d**) EDS spectrum of the CTO:0.02Pr, 0.02Sn phosphor.

3.1.2. Photoluminescence Properties

As shown in Figure 2a, characteristic transitions of Pr^{3+} ions were observed in the excitation spectra and the emission spectrum of CTO:0.02Pr. When monitored at 487 and 617 nm, respectively, the excitation spectra were similar in shape, indicating that both emissions originated from the same Pr^{3+} center. Typical excitation bands contributing to the 4f-4f transitions of Pr^{3+} were observed at 450 nm, 470 nm, and 486 nm. A broad excitation band in the UV region was also found, which could be assigned to the overlapping of the host-related absorption and IVCT bands. Under 450 nm excitation, the strongest emission band was found at 487 nm. The intense cyan–greenish emission could be ascribed to the $^3P_0 \rightarrow {}^3H_4$ transition of Pr^{3+}. Moreover, the sample also exhibited other characteristic emissions of Pr^{3+}, including $^3P_1 \rightarrow {}^3H_5$, $^3P_0 \rightarrow {}^3H_5$, $^1D_2 \rightarrow {}^3H_4$, $^3P_0 \rightarrow {}^3H_6$, and $^3P_0 \rightarrow {}^3F_2$. The corresponding schematic energy-level diagram of Pr^{3+} in CTO is illustrated in Figure 2b. There is obvious splitting in the emission bands of $^3P_0 \rightarrow {}^3H_4$, $^1D_2 \rightarrow {}^3H_4$, $^3P_0 \rightarrow {}^3H_6$, and $^3P_0 \rightarrow {}^3F_2$, suggesting that Pr^{3+} occupies a low-symmetry local environment in the CTO lattice.

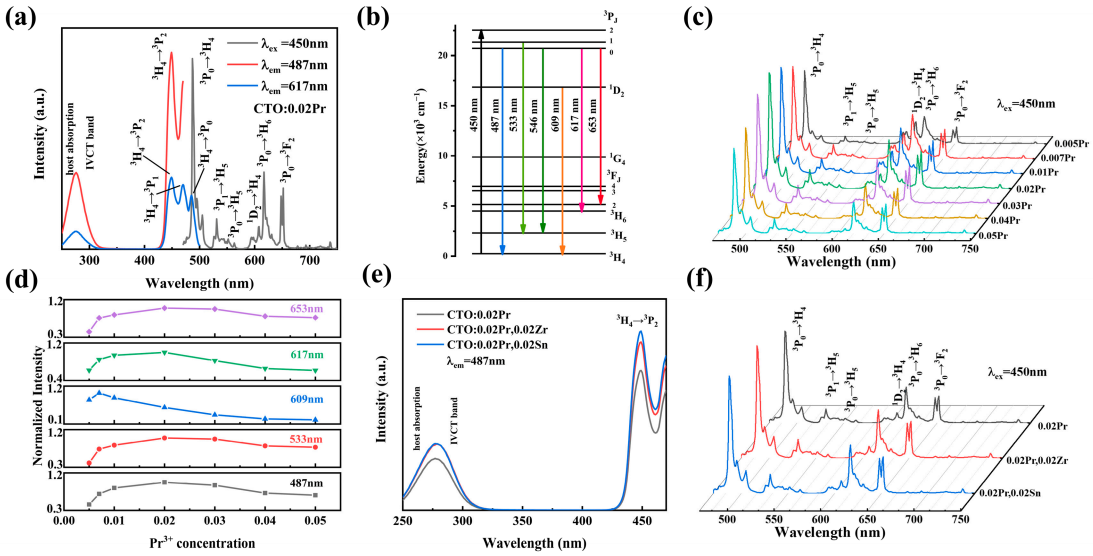


Figure 2. (**a**) Excitation and emission spectra of the CTO:0.02Pr sample; (**b**) schematic energy-level diagram of CTO:Pr^{3+}; (**c**) emission spectra of CTO:*x*Pr (*x* = 0.005–0.05) under 450 nm excitation; (**d**) normalized integrated emission intensities of different emission bands marked by the wavelength at the intensity maximum; (**e**) excitation and (**f**) emission spectra of CTO:0.02Pr and CTO:0.02Pr, 0.02M (M = Zr and Sn).

The emission spectra of CTO phosphors varying with Pr^{3+} concentrations are shown in Figure 2c. Similar spectral profiles are observed in them, indicating that the luminescence centers and their local environments remained essentially unchanged within the investigated concentration range. The concentration-dependent emission intensity is summarized in Figure 2d. The concentration-induced quenching at the $^1D_2$ level (0.7 mol%) was found to occur at a lower Pr^{3+} doping concentration compared to that (2 mol%) at the ^3P_J levels (J = 1 or 0). This phenomenon could be explained by their different responses induced by the energy migration and cross-relaxation processes [21–23]. The CIE chromaticity coordinates of the CTO phosphors with different Pr^{3+} concentrations are shown in Figure S1 and Table S1. With increasing Pr^{3+} concentrations, the emission color gradually shifts from the orange–red region ((x, y) = (0.436, 0.370)) toward the yellow–green region ((x, y) = (0.326, 0.399)). This behavior is consistent with the different concentration quenching characteristics of the $^1D_2$ and ^3P_J levels.

The excitation and emission spectra of the CTO:0.02Pr and CTO:0.02Pr, 0.02M (M = Zr and Sn) phosphors are shown in Figures 2e and 2f, respectively. In comparison with the singly Pr^{3+}-doped samples, there was apparently stronger emission in the samples with Pr^{3+}/Zr^{4+} or Pr^{3+}/Sn^{4+} co-doping under 450 nm excitation. The emission intensity in CTO:0.02Pr, 0.02Zr, and CTO:0.02Pr, 0.02Sn was 1.31 times and 1.34 times that in CTO:0.02Pr, respectively. The enhancement could mainly be ascribed to improved charge compensation, which suppresses the defect-related nonradiative relaxation induced by the substitution of Ca^{2+} by Pr^{3+} [24]. In addition, charge compensation might also contribute to the stabilization of the local coordination environment around Pr^{3+} [25]. The better performance of the sample co-doped with Sn could further be related to possible valence regulation during sintering, leading to an increased population of effective Pr^{3+} luminescence centers.

3.1.3. Temperature-Dependent Photoluminescence and Optical Thermometric Performance

The emission spectra at different environmental temperatures from 298 to 573 K were measured in the CTO:0.02Pr, 0.02Sn sample under 450 nm excitation, as shown in Figure 3a. It was selected because it exhibited the most intense emission among all obtained samples.

Most emissions were found to be quenched with the rising of the temperature. Figure 3b shows the temperature-dependent integrated intensities of four characteristic emission bands at 487, 533, 609, and 653 nm, corresponding to the transitions of $^3P_0 \rightarrow {}^3H_4$, $^3P_1 \rightarrow {}^3H_5$, $^1D_2 \rightarrow {}^3H_4$, and $^3P_0 \rightarrow {}^3F_2$, respectively. It can be seen that there was more significant thermal quenching in the $^3P_0$-related emissions as compared to the $^3P_1$- or $^1D_2$-related emissions. The CIE chromaticity coordinates at different temperatures are shown in Figure S2 and Table S2. With the increasing temperature, the emission color of CTO:0.02Pr, 0.02Sn gradually shifted toward the orange–red region.

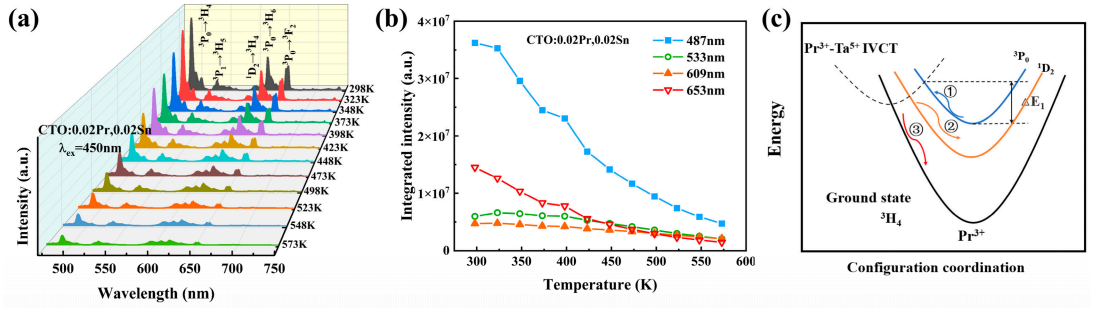


Figure 3. (**a**) Temperature-dependent emission spectra of the CTO:0.02Pr,0.02Sn phosphor; (**b**) the integrated intensities of different emission bands marked by the wavelength at the intensity maximum; (**c**) configuration coordinate diagram of the nonradiative relaxation processes of Pr^{3+}during heating: ① $^3P_0 \rightarrow$IVCT; ② IVCT$\rightarrow {}^1D_2$; ③ IVCT$\rightarrow {}^3H_4$.

The thermal quenching at the $^3P_0$ level is affected not only by the thermally coupled levels but also by nonradiative processes associated with the $^3P_0$ and $^1D_2$ levels. Previous studies have shown that the thermal quenching behavior at this level is strongly affected by the IVCT state [26–31]. A schematic diagram is provided in Figure 3c for better explanation. When excited at 450 nm, the electrons in the ground $^3H_4$ state are firstly populated to the $^3P_0$ excited state. Then, electrons located at the $^3P_0$ excited state can acquire sufficient energy from thermal phonons with increasing temperatures. It overcomes the energy barrier ΔE_1 and transfer to the Pr^{3+}-Ta^{5+} IVCT state (process ①). Upon reaching the IVCT state, the electrons tend to relax toward lower-lying levels. Since the energy barrier between the IVCT state and the $^3P_0$ level is significantly higher than that between the IVCT state and the $^1D_2$ level, the electrons more readily relax to the $^1D_2$ level (process ②) rather than returning to the $^3P_0$ level, and some of them further relax to the $^3H_4$ ground state (process ③). As a result, the population of the $^3P_0$ level would continuously decrease with the rising temperature, leading to the pronounced thermal quenching of the $^3P_0$-related emissions at high temperatures. In contrast, the $^1D_2$ level can be partially replenished by the relaxation process from the $^3P_0$ level and therefore exhibits comparatively weaker thermal quenching.

Since different emission bands exhibit different temperature dependences, suitable emission pairs can be further selected to construct the FIR parameter. To evaluate the thermometric performance of the CTO:0.02Pr, 0.02Sn phosphor, three FIR modes were employed as temperature-sensitive signals. They were $^3P_1 \rightarrow {}^3H_5/{}^3P_0 \rightarrow {}^3H_4$, $^3P_1 \rightarrow {}^3H_5/{}^3P_0 \rightarrow {}^3F_2$, and $^1D_2 \rightarrow {}^3H_4/{}^3P_0 \rightarrow {}^3H_4$. The FIR–temperature relationship was fitted using the following equation [32]:

$$FIR = Aexp\left(-\frac{\Delta E}{k_B T}\right) + C = Aexp\left(-\frac{B}{T}\right) + C \quad (1)$$

where ΔE, T, and k_B represent the energy difference, absolute temperature, and Boltzmann constant, respectively. A and C are the fitted curve's relevant constant parameters, with A associated with the spontaneous emission rate, degeneracy, and angular frequency. $\Delta E/k_B$

is denoted as B to simplify the formula. The absolute sensitivity (S_a) and relative sensitivity (S_r) can be further derived as follows:

$$S_a = \left|\frac{dFIR}{dT}\right| = \frac{B}{T^2} \times A \times exp\left(-\frac{B}{T}\right) \quad (2)$$

$$S_r = \left|\frac{1}{FIR}\frac{dFIR}{dT}\right| = \frac{B}{T^2} \times \frac{Aexp\left(-\frac{B}{T}\right)}{Aexp\left(-\frac{B}{T}\right)+C} \quad (3)$$

As shown in Figure 4a, in the CTO:0.02Pr, 0.02Sn phosphor, the FIR based on $^3P_1 \rightarrow {}^3H_5/{}^3P_0 \rightarrow {}^3F_2$ was well fitted as a function of the temperature. As shown in Figure 4b, it exhibits maximum relative sensitivity of 1.09% K^{-1} at 298 K. This is much higher than that of the other two FIR modes based on $^3P_1 \rightarrow {}^3H_5/{}^3P_0 \rightarrow {}^3H_4$ and $^1D_2 \rightarrow {}^3H_4/{}^3P_0 \rightarrow {}^3H_4$, as presented in Figure S3. Moreover, temperature resolution (δT) is an important criterion for evaluating the sensing performance of optical thermometers. It is defined as the minimum temperature resolvable by the thermometer, depending not only on the material but also on the experimental environment used, such as the detection setup, acquisition conditions, and signal-to-noise ratio. Temperature resolution is given by the following equation [12]:

$$\delta T = \Delta T = \frac{\delta FIR}{S_a} = \frac{1}{S_r}\frac{\delta FIR}{FIR} \quad (4)$$

where δFIR is the standard deviation of FIR. $\delta FIR/FIR$ is the relative error, which is determined by multiple emission spectral measurements at a single temperature. Here, the emission spectra were measured ten times at room temperature to calculate the relative error for the entire temperature range. The temperature resolution δT for the FIR of $^3P_1 \rightarrow {}^3H_5/{}^3P_0 \rightarrow {}^3F_2$ at 298–573 K was estimated to be 0.64–0.99 K, as shown in Figure 4c. Then, heating–cooling cycle measurements were carried out, and the corresponding FIR values are presented in Figure 4d. The reproducibility R was calculated according to the following equation:

$$R = 1 - \max\left|\frac{FIR_i - FIR_{av}}{FIR_{av}}\right| \quad (5)$$

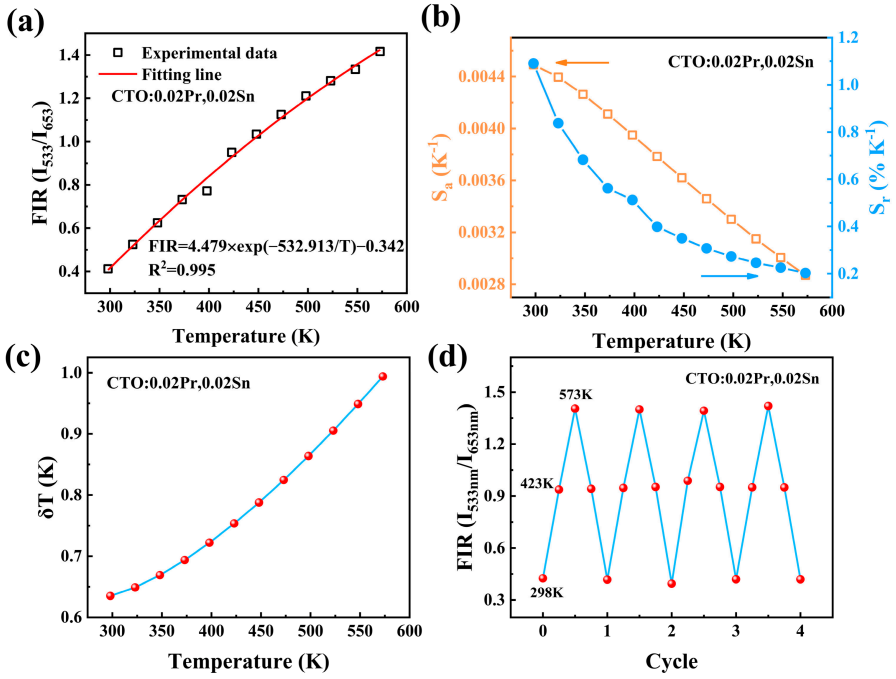


Figure 4. (**a**) FIR fitting curve; (**b**) the corresponding relative and absolute sensitivity curves; (**c**) temperature uncertainty (δT) as a function of temperature; and (**d**) temperature cycling of FIR between 298 and 573 K in the CTO:0.02Pr, 0.02Sn phosphor.

The reproducibility R reached 98.8%, 98.4%, and 98.9% at 298, 423, and 573 K, respectively, indicating that the FIR response remains highly stable and reproducible during thermal cycling.

3.2. $CaTa_2O_6:Pr^{3+}$ PiG

3.2.1. Phase Structure and Morphology

Figure 5a shows the DSC curve of 30Zn30Bi40B-PG, from which the glass transition temperature (T_g), crystallization onset temperature (T_x), and crystallization peak temperature (T_p) were determined to be 417, 569, and 593 °C, respectively. The characteristic temperatures are low enough to ensure an acceptable softening point. The 30Zn30Bi40B glass is expected to offer good thermal processability, thereby minimizing the risk of phosphor degradation and interfacial reactions during co-sintering.

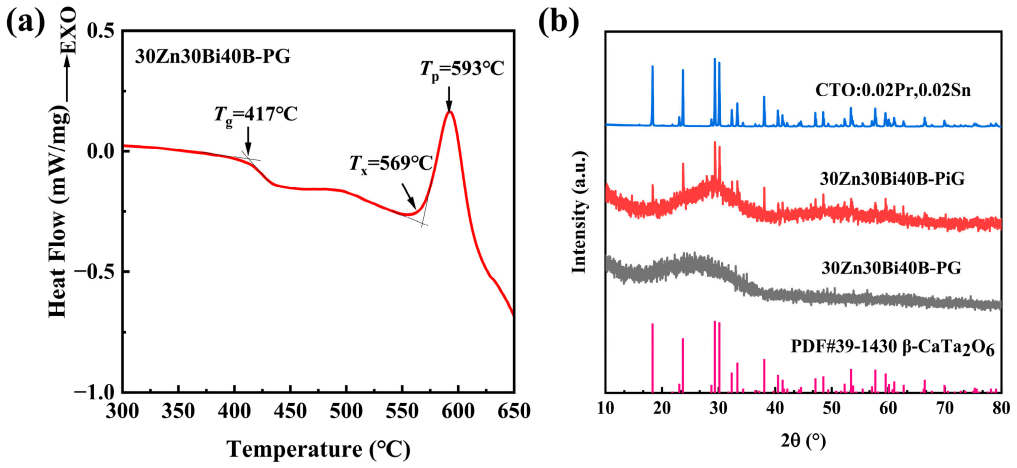


Figure 5. (**a**) DSC curve of 30Zn30Bi40B-PG; (**b**) XRD patterns of the PG, CTO:0.02Pr,0.02Sn phosphor, and corresponding PiG sample.

Figure 5b shows the XRD patterns of the PG, CTO:0.02Pr, 0.02Sn phosphor and the PiG sample. The PG exhibits a typical non-crystalline profile, in agreement with the nature of its amorphous structure. The phosphor sample shows sharp diffraction peaks, which matches well with the standard pattern of β-$CaTa_2O_6$ (PDF#39-1430). In the PiG sample, the characteristic diffraction peaks of β-$CaTa_2O_6$ with a background of non-crystallinity were observed. No extra diffraction peaks assignable to impurity phases were detected. This suggests that the phosphor was successfully incorporated.

The morphology of the PiG sample was analyzed by SEM and EDS. The sample was treated with a 10 vol% HF solution for 5 s at first, and then Pt nanoparticles were sprayed on the surface for measurement. As shown in Figure 6a, the phosphor particles were embedded in the glass matrix and remained clearly distinguishable. The dark areas reflect the crystalline phase, while the bright areas reflect the remained glass phase after HF etching. The results of EDS line scanning crossing the interface between the phosphor particle and the glassy matrix are given in Figure 6b. Elements of Ta, Pr, and Sn were found to be concentrated in the phosphor particle region, while Bi and Zn were enriched in the glass region. This suggests that phosphor degradation and interfacial reactions were controlled during co-sintering.

EDS point analyses were further carried out in the phosphor particle region, the glass region, and their interface. The results are shown in Figure 6c–e, respectively. In the phosphor particle region, elements of O, Ca, Ta, Pr, and Sn dominated (Figure 6c), whereas O, Bi, and Zn were found in the glass region (Figure 6d). At their interface, all elements mentioned above were detected (Figure 6e), indicating that there should be an interfacial

transition layer between the phosphor particle and the glass matrix. The high F content observed at the interface suggests that the region exhibits much weaker chemical stability against HF etching. It indicates that there was an undesirable interfacial reaction during PiG fabrication, which might result in photoluminescence quenching at high temperatures. Upon carefully checking the elemental distributions of Bi, Ca, and Ta found in Figure 6b, the above-mentioned phenomenon could be mainly ascribed to the mutual diffusion of Bi and Ca during PiG fabrication.

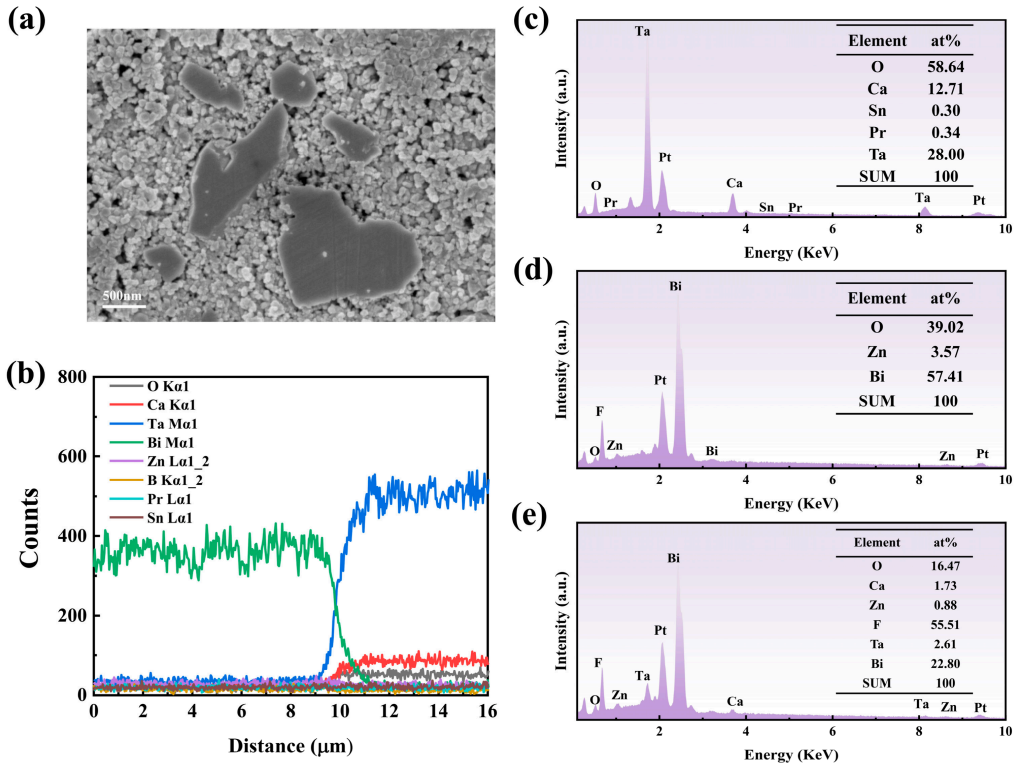


Figure 6. (**a**) SEM image showing the distribution of phosphor particles and the glass matrix; (**b**) EDS line analysis profile across a phosphor particle and the adjacent glass region; EDS point analysis results for the (**c**) phosphor particle, (**d**) glass matrix, and (**e**) interfacial region, respectively.

3.2.2. Optical Properties

Figure 7a shows the transmittance spectrum of the PG and the diffuse reflectance spectrum of the CTO:0.02Pr, 0.02Sn phosphor. The transmission window of the PG overlaps well with the characteristic absorption bands of Pr^{3+} ions in the phosphor, especially in the 450–500 nm range. This indicates that the visible-light excitation can be effectively transmitted through the glassy encapsulation and arrive at the surfaces of the phosphor particles. As shown in Figure 7b, the excitation bands and emission bands assigned to the characteristic transitions of Pr^{3+} ions were observed in the PiG sample, which were very similar to those found in the CTO:0.02Pr, 0.02Sn phosphor. No obvious peak position shifting in the PiG was found in comparison to the phosphor. However, the host-related broad-band absorption and the IVCT excitation band in the ultraviolet region are almost invisible. This is mainly due to the stronger UV absorption of the PG. On the whole, the PiG should be suitable for blue-light excitation.

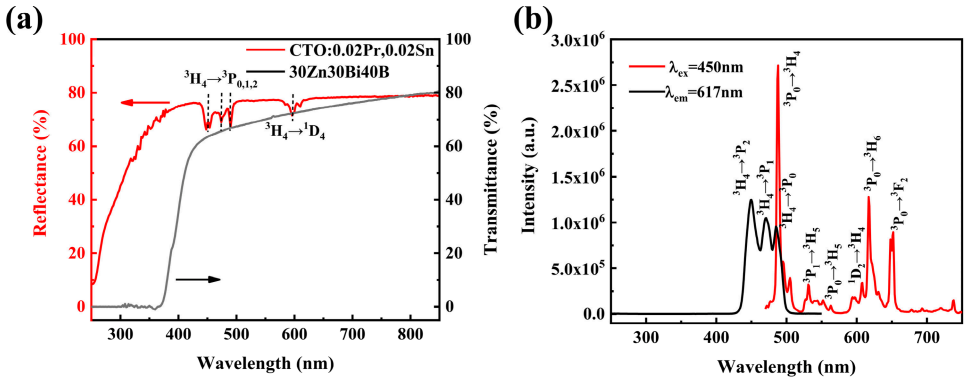


Figure 7. (**a**) Transmittance spectrum of the PG and diffuse reflectance spectrum of the CTO:0.02Pr, 0.02Sn phosphor; (**b**) excitation and emission spectra of the 30Zn30Bi40B-PiG sample.

3.2.3. Temperature-Dependent Photoluminescence and Optical Thermometric Performance

Figure 8a shows the temperature-dependent emission spectra of the PiG sample under 450 nm excitation. It can be seen that the intensities of all characteristic emissions gradually decrease with increasing temperatures, indicating obvious thermal quenching during the heating process. The integrated intensities of the characteristic emission bands at 487 nm, 533 nm, 609 nm, and 653 nm as a function of the temperature are given in Figure 8b. They are in correspondence with the transitions of $^3P_0 \rightarrow {}^3H_4$, $^3P_1 \rightarrow {}^3H_5$, $^1D_2 \rightarrow {}^3H_4$, and $^3P_0 \rightarrow {}^3F_2$, respectively. In comparison with the phosphor, the emission intensity of the PiG dropped rapidly with the rising temperature. The CIE coordinates of the PiG sample at different temperatures are shown in Figure S4 and Table S3. This phenomenon might be ascribed to the phosphor/glass interface. Local structural distortion, coordination variation, and possible defect centers near the interface may serve as thermally activated nonradiative relaxation channels, thereby accelerating energy dissipation and leading to faster emission decay at elevated temperatures [33,34]. This indicates that the PiG might only be suitable for optical thermometry in low-to-moderate temperature ranges.

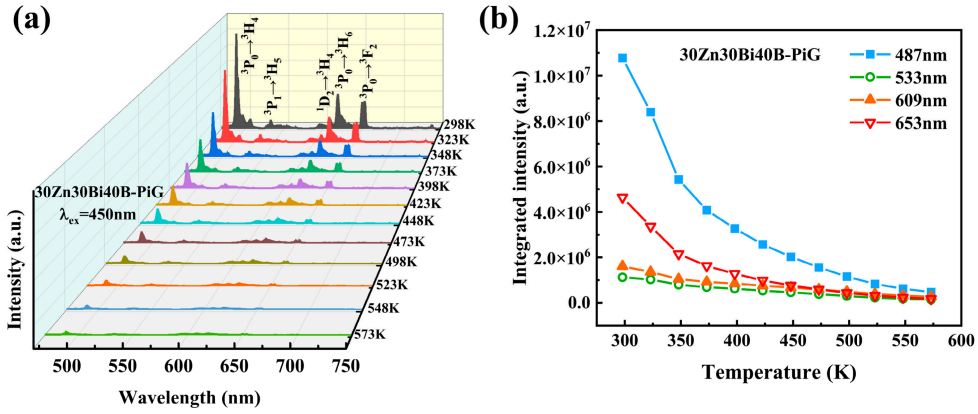


Figure 8. (**a**) Temperature-dependent emission spectra of 30Zn30Bi40B-PiG recorded from 298 to 573 K and (**b**) the corresponding integrated intensities of the characteristic emission bands.

Similarly to the CTO:0.02Pr, 0.02Sn phosphor, the optical thermometric performance of 30Zn30Bi40B-PiG was also evaluated, using the FIR based on the $^3P_1 \rightarrow {}^3H_5/{}^3P_0 \rightarrow {}^3F_2$ transition pair, which shows the highest relative sensitivity among the investigated modes. As shown in Figure 9a,b, this FIR mode can be well fitted as a function of the temperature and exhibits maximum relative sensitivity of 1.18% K^{-1} at 298 K, which is slightly higher than that of the corresponding phosphor. The other two FIR modes are presented in Figure S5. The corresponding temperature uncertainty δT remains within 0.78–1.56 K

over 298–573 K (Figure 9c), indicating acceptable temperature resolution. In addition, the heating–cooling cycle test (Figure 9d) gives reproducibility values of 98.9%, 99.0%, and 99.1% at 298, 423, and 573 K, respectively, confirming the good stability and repeatability of the FIR response. These results suggest that the thermometric mechanism governed by the combined effects of thermally coupled levels and IVCT-related nonradiative channels of Pr^{3+} remains in the PiG sample, although there is increased nonradiative relaxation due to the phosphor/glass interface.

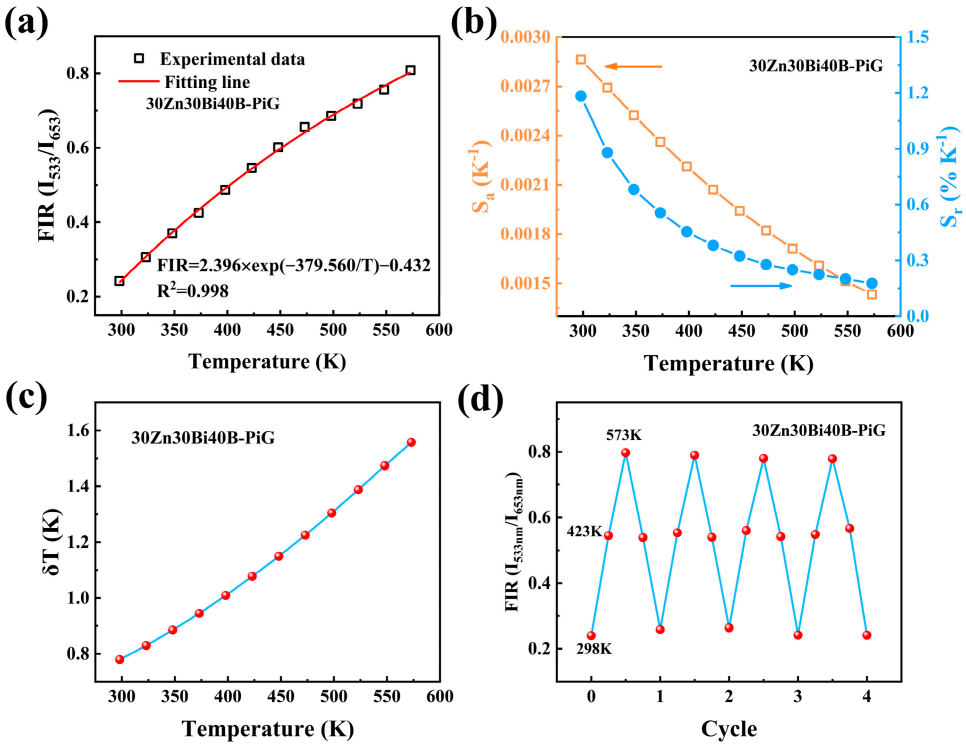


Figure 9. (**a**) FIR fitting curve; (**b**) the corresponding relative and absolute sensitivity curves; (**c**) temperature uncertainty (δT) as a function of temperature; and (**d**) temperature cycling of FIR between 298 and 573 K in 30Zn30Bi40B-PiG.

As summarized in Table 1, the $CaTa_2O_6$:Pr^{3+} phosphor and the PiG based on it exhibit competitive thermometric performance in comparison with those reported in various Pr^{3+}-activated luminescent thermometers. A relative sensitivity maximum of 1.09% K^{-1} at 298 K in the 298–573 K temperature range is found in the CTO:0.02Pr, 0.02Sn phosphor. The PiG sample achieves a relative sensitivity maximum of 1.18% K^{-1} at 298 K. These results indicate that $CaTa_2O_6$:Pr^{3+}-based materials are promising candidates for luminescence thermometry.

Table 1. The maximum relative sensitivities of Pr^{3+}-doped optical sensing materials.

Host Material	Transitions	Range (K)	$S_{r\text{-}Max}$ (% K^{-1})	Ref.
$NaCaY(MoO_4)_3$	$^3P_1 \rightarrow {}^3H_5/{}^3P_0 \rightarrow {}^3F_2$	298–498	1.2 (298 K)	[35]
$Ca_3Y_2Si_3O_{12}$	$^3P_0 \rightarrow {}^3H_4/P_1 \rightarrow {}^3H_5$	298–573	0.744 (298 K)	[36]
$CaTiO_3$	$^1D_2 \rightarrow {}^3H_4/{}^1D_2 \rightarrow {}^3H_4$	20–200	0.82 (120 K)	[37]
$Sr_3Y_2Ge_3O_{12}$	$^3P_0 \rightarrow {}^3H_4/{}^1D_2 \rightarrow {}^3H_4$	13–1025	0.78 (188 K)	[38]
$CaTa_2O_6$ phosphor	$^3P_1 \rightarrow {}^3H_5/{}^3P_0 \rightarrow {}^3F_2$	298–573	1.09 (298 K)	This work
$CaTa_2O_6$ PiG	$^3P_1 \rightarrow {}^3H_5/{}^3P_0 \rightarrow {}^3F_2$	298–573	1.18 (298 K)	This work

4. Conclusions

The luminescence properties and optical temperature sensing performance of $CaTa_2O_6$:Pr^{3+} phosphors under blue-light excitation have been reported. The ICVT band is confirmed in the photoluminescence excitation spectrum. Under excitation at 450 nm, the optimal Pr^{3+} doping concentration is found to be 2 mol% and 0.7 mol% for the emissions from the ^3P_J levels and the $^1D_2$ level, respectively. Upon co-doping with Zr or Sn, the emission intensity is enhanced to 1.31 times and 1.34 times that in the Pr single-doped phosphor. Furthermore, a PiG composite was fabricated based on the CTO:0.02Pr, 0.02Sn phosphor, which exhibits a similar spectral profile regarding both the excitation and emission spectra to the phosphor. Employing the differences in the thermal-dependent photoluminescence spectra, an FIR mode based on $^3P_1 \rightarrow {}^3H_5/{}^3P_0 \rightarrow {}^3F_2$ was found to be promising for optical temperature sensing. Relative sensitivity maxima of 1.09% K^{-1} and 1.18% K^{-1} at 298 K were found in the phosphor and the PiG under 450 nm excitation, respectively. $CaTa_2O_6$:Pr^{3+}-based materials show potential for luminescence thermometry.

Supplementary Materials: The following supporting information can be downloaded at https://www.mdpi.com/article/10.3390/ma19112324/s1. Figure S1: CIE chromaticity coordinates of CTO phosphors with different Pr^{3+} concentrations; Table S1: CIE chromaticity coordinates of CTO phosphors with different Pr^{3+} concentrations; Figure S2: CIE chromaticity coordinates of CTO:0.02Pr, 0.02Sn phosphor at different temperatures; Table S2: CIE chromaticity coordinates of CTO:0.02Pr, 0.02Sn phosphor at different temperatures; Figure S3: (a,c) FIR fitting curves and (b,d) the corresponding relative and absolute sensitivity curves of the CTO:0.02Pr, 0.02Sn phosphor. (a,b) $^3P_1 \rightarrow {}^3H_5/{}^3P_0 \rightarrow {}^3H_4$; (c,d) $^1D_2 \rightarrow {}^3H_4/{}^3P_0 \rightarrow {}^3H_4$; Figure S4: CIE chromaticity coordinates of PiG at different temperatures; Table S3: CIE chromaticity coordinates of PiG phosphor at different temperatures; Figure S5: (a,c) FIR fitting curves and (b,d) the corresponding relative and absolute sensitivity curves of the PiG. (a,b) $^3P_1 \rightarrow {}^3H_5/{}^3P_0 \rightarrow {}^3H_4$; (c,d) $^1D_2 \rightarrow {}^3H_4/{}^3P_0 \rightarrow {}^3H_4$.

Author Contributions: Conceptualization, Q.J. and J.R.; methodology, Q.J.; validation, Q.J., J.R. and C.T.; formal analysis, Q.J. and J.R.; investigation, Q.J., Z.Z., S.Z. and J.R.; data curation, Q.J. and J.R.; writing—original draft preparation, Q.J. and J.R.; writing—review and editing, J.R., C.T. and C.L.; visualization, Q.J.; supervision, J.R. and C.T.; project administration, J.R.; funding acquisition, J.R., C.T. and C.L.; J.R., C.T., Z.Z., S.Z. and C.L. contributed to experimental assistance, characterization, and data discussion. All authors have read and agreed to the published version of the manuscript.

Funding: This work was supported by the Fundamental Research Funds for the Central Universities, China (WUT: 2018-III-017, 2020-III-20); the Hubei Provincial Natural Science Foundation of China (No. 2015CFB648); the 111 Project, China (No. B18038); and the Postdoctoral Independent Innovation Fund of Wuhan University of Technology (WUT: 3120625135).

Institutional Review Board Statement: Not applicable.

Informed Consent Statement: Not applicable.

Data Availability Statement: The original contributions presented in this study are included in the article/supplementary material. Further inquiries can be directed to the corresponding authors.

Acknowledgments: The authors gratefully acknowledge Xiujian Zhao, Jianjun Han, and Haizheng Tao of Wuhan University of Technology and Yang Li of Guangzhou Medical University for their helpful discussions during this work.

Conflicts of Interest: The authors declare no conflicts of interest.

References

1. Li, L.; Zi, L.; Yang, F.; Feng, S.; Wang, C.; Yang, Y. Pr^{3+}-Based Visible-to-Ultraviolet Upconversion. A Minireview. *Adv. Phys. Res.* **2025**, *4*, 2400097. [CrossRef]
2. Shen, T.; Zhao, S.; Su, A.; Liu, H.; Chen, F.; Li, B.; Han, X.; Yu, D.; Zhang, D. Visible/near-Infrared Luminescence and Concentration Effects of Pr^{3+}-Doped $Sr_2Al_2GeO_7$ Downconversion Phosphors. *APL Mater.* **2024**, *12*, 091103. [CrossRef]
3. Sójka, M.; Ramalho, J.F.C.B.; Brites, C.D.S.; Fiaczyk, K.; Carlos, L.D.; Zych, E. Bandgap Engineering and Excitation Energy Alteration to Manage Luminescence Thermometer Performance. The Case of $Sr_2(Ge,Si)O_4:Pr^{3+}$. *Adv. Opt. Mater.* **2019**, *7*, 1901102. [CrossRef]
4. Lou, Y.; Tian, Z.; Hu, Q.; Bai, Y.; Deng, Q.; Zou, B.; Chen, X.; Yuan, M.; Zeng, R. Multi-Modal Luminescence in Rare Earth-Doped Double Perovskite Oxides and Highly Thermal Sensitivity from Coupled Energy Levels. *J. Alloys Compd.* **2025**, *1036*, 182086. [CrossRef]
5. Aly Taleb, Z.E.A.; Saidi, K.; Dammak, M. Dual-Mode Optical Ratiometric Thermometry Using Pr^{3+}-Doped $NaSrGd(MoO_4)_3$ Phosphors with Tunable Sensitivity. *Dalton Trans.* **2023**, *52*, 18069–18081. [CrossRef]
6. Gheorghe, C.; Hau, S.; Stanciu, G.; Avram, D.; Broasca, A.; Gheorghe, L. Novel Optical Temperature Sensors Based on the Emission of the Pr^{3+} Ions Doped $Ca_3(M,Ga)_5O_{12}$ (M^{5+} = Nb, Ta) Garnet Phosphors. *J. Alloys Compd.* **2022**, *922*, 166178. [CrossRef]
7. Chen, Y.; Zhao, F.; Qiang, K.; Mao, Q.; Yang, H.; Zhu, Y.; Liu, M.; Zhong, J. Self-Calibrated Thermometer and Dynamic Anti-Counterfeiting Based on $YNbO_4:Pr^{3+}$ Luminescent Material. *Adv. Opt. Mater.* **2024**, *12*, 2401688. [CrossRef]
8. Tang, W.; Zuo, C.; Li, Y.; Ma, C.; Yuan, X.; Wen, Z.; Cao, Y. Exploiting Intervalence Charge-Transfer Engineering to Finely Control $(Ba, Sr)TiO_3:Pr^{3+}$ Luminescence Thermometers. *J. Lumin.* **2021**, *236*, 118103. [CrossRef]
9. Ueda, K.; Oya, A.; Nagashima, S.; Ogata, T.; Honma, T.; Omata, T. Site-Dependent Luminescence from Pr^{3+} in Double-Perovskite-Type Alkaline Earth Lanthanum Tantalates. *J. Phys. Chem. C* **2023**, *127*, 8833–8839. [CrossRef]
10. Tian, C.; Ruan, J.; Zhao, X.; Han, J.; Liu, C. Infrared Transparent $CaO\text{-}Ta_2O_5\text{-}Al_2O_3$ Glass-Ceramics with High Microhardness: Crystallization Behavior and Microstructure Development. *Ceram. Int.* **2024**, *50*, 10465–10475. [CrossRef]
11. Teixeira, N.G.; Moreira, R.L.; Lobo, R.P.S.M.; Andreeta, M.R.B.; Hernandes, A.C.; Dias, A. Raman and Infrared Phonon Features in a Designed Cubic Polymorph of $CaTa_2O_6$. *Cryst. Growth Des.* **2011**, *11*, 5567–5573. [CrossRef]
12. Tian, C.; Ruan, J.; Zhao, X.; Han, J.; Liu, C. Structure, Spectroscopic Properties and Optical Temperature-Sensing Behavior of Glass-Ceramics Containing Polymorphic $CaTa_2O_6:Er^{3+}/Yb^{3+}$ Nanocrystals. *J. Mater. Chem. C* **2024**, *12*, 16594–16607. [CrossRef]
13. Tian, C.; Ruan, J.; Cheng, Y.; Zhao, X.; Han, J.; Liu, C. Ni^{2+} Concentration-Dependent and Temperature-Dependent NIR Photoluminescence Properties in Novel Transparent Glass-Ceramics Containing Cubic $CaTa_2O_6:Ni^{2+}$ Nanocrystals. *Ceram. Int.* **2024**, *50*, 54379–54389. [CrossRef]
14. Noto, L.L.; Chithambo, M.L.; Ntwaeaborwa, O.M.; Swart, H.C. The Greenish-Blue Emission and Thermoluminescent Properties of $CaTa_2O_6:Pr^{3+}$. *J. Alloys Compd.* **2014**, *589*, 88–93. [CrossRef]
15. Yang, C.; Xin, Y.; Liu, J.; Zhao, Y.; Ouyang, R.; Guo, N. Defect Compensation and Intervalence Charge Transfer State-Based Pr^{3+}-Doped Niobate Antithermal Quenching Phosphors. *Chem. Commun.* **2024**, *60*, 6687–6690. [CrossRef]
16. Zhong, L.; Jiang, S.; Wang, X.; Li, Y.; Wang, Y.; Xie, J.; Ling, F.; Wang, Y.; Xiang, G.; Li, L.; et al. Dual-Mode Optical Thermometry Based on Intervalence Charge Transfer Excitations in Tb^{3+}/Pr^{3+} Co-Doped $CaNb_2O_6$ Phosphors. *Ceram. Int.* **2022**, *48*, 30005–30011. [CrossRef]
17. Li, Y.; Li, X.; Luo, J.; Liu, Z.; Cheng, L.; Yu, H.; Wang, Y.; Xu, S.; Chen, B. Visible to Near-Infrared Emissions of $Bi_2Mo_2O_9:Pr^{3+}$ Multifunctional Phosphors for Multi-Mode Temperature Sensing, White LEDs and Bioimaging. *Spectrochim. Acta Part A Mol. Biomol. Spectrosc.* **2025**, *330*, 125673. [CrossRef] [PubMed]
18. Chung, W.J.; Nam, Y.H. Review—A Review on Phosphor in Glass as a High Power LED Color Converter. *ECS J. Solid State Sci. Technol.* **2020**, *9*, 016010. [CrossRef]
19. Shannon, R.D. Revised effective ionic radii and systematic studies of interatomic distances in halides and chalcogenides. *Acta Crystallogr. Sect. A* **1976**, *32*, 751–767. [CrossRef]
20. Su, H.; Li, X.; Li, D.; Gao, D.; Zhang, M.; Shang, Y.; Liu, Y.; Geng, H.; Liu, X.; Yu, R. Strategic Point Defect Engineering toward Abnormal Thermal Quenching in Sm^{3+}-Doped Na-Rich $Na_{1.5}La_{1.5}TeO_6$ Phosphors for LEDs Applications. *Ceram. Int.* **2024**, *50*, 34111–34122. [CrossRef]
21. Wang, T.; Su, C.; Zhang, H.; Bao, W.; Wang, Q. Pr^{3+}-Er^{3+} Co-Doped $Ba_{3.75}Gd_{0.833}Nb_{10}O_{30}$ Glass-Ceramics for Tunable Luminescence, Optical Anti-Counterfeiting and Temperature Sensing. *Ceram. Int.* **2024**, *50*, 4907–4920. [CrossRef]
22. Liu, C.; Pan, F.; Peng, Q.; Zhou, W.; Shi, R.; Zhou, L.; Zhang, J.; Chen, J.; Liang, H. Excitation Wavelength Dependent Luminescence of $LuNbO_4:Pr^{3+}$—Influences of Intervalence Charge Transfer and Host Sensitization. *J. Phys. Chem. C* **2016**, *120*, 26044–26053. [CrossRef]
23. Naresh, V.; Ham, B.S. Influence of Multiphonon and Cross Relaxations on $^3P_0$ and $^1D_2$ Emission Levels of Pr^{3+} Doped Borosilicate Glasses for Broad Band Signal Amplification. *J. Alloys Compd.* **2016**, *664*, 321–330. [CrossRef]

24. Yao, C.; Zhang, C. Photoluminescence Enhancement and Excellent Thermal Stability of $Ca_2ZnSi_2O_7$:Pr^{3+} Red-Emitting Phosphors through Charge Compensator A^+ (Li^+, Na^+ and K^+) Co-Doping for w-LED Applications. *Spectrochim. Acta Part A Mol. Biomol. Spectrosc.* **2023**, *303*, 123177. [CrossRef]
25. Hou, D.; Huang, R.; Zhang, Y.; Li, H.; Zhang, W.; Lin, Z.; Guo, Y.; Lin, Z.; Dong, J.; Li, J.-Y. Multi-Band Emission of Pr^{3+}-Doped $Ca_3Al_2O_6$ and the Effects of Charge Compensator Ions on Luminescence Properties. *Nanomaterials* **2023**, *14*, 2. [CrossRef]
26. Anu; Rao, A.S. Luminescence and Optical Thermometry Strategy Based on Emission Spectra of $Li_2Ba_5W_3O_{15}$:Pr^{3+} Phosphors. *Opt. Mater.* **2023**, *145*, 114476. [CrossRef]
27. Liu, J.; Xin, Y.; Qu, S.; Yang, C.; Song, J.; Li, W.; Guo, N. Design of Dual-Mode Optical Thermometry Based on Thermally Activated Efficient Energy Transfer in $LaNbO_4$/Ln^{3+} (Eu^{3+}/Sm^{3+}/Pr^{3+}) Phosphors. *ACS Appl. Mater. Interfaces* **2024**, *16*, 57421–57427. [CrossRef] [PubMed]
28. Lv, X.; Guo, N.; Lv, W.; Liu, R.; Qu, S.; Ouyang, R. Regulating Luminescence Thermal Quenching of Praseodymium-Doped Niobo-Tantalate Phosphor through Intervalence Charge Transfer Band Displacement. *Inorg. Chem.* **2023**, *62*, 15747–15756. [CrossRef] [PubMed]
29. Qiu, W.; Cao, H.; Gao, L.; Yan, Z.; Zhao, Y.; Chen, Y.; Liu, C.; Guo, N. Tailoring intervalence charge transfer band position to suppress thermal quenching in $Mg_{1-x}Ca_xNb_2O_6$:Pr^{3+} phosphors. *Ceram. Int.* **2026**, *52*, 13488–13494. [CrossRef]
30. Chai, H.; Yang, C.; Liu, J.; Lv, X.; Xiao, R.; Li, W.; Song, J.; Zhao, J.; Guo, N. Improving the Thermal Stability of Pr^{3+}-Based Niobate Phosphor by Adjusting the Energy Level of Intervalence Charge Transfer Band. *Ceram. Int.* **2025**, *51*, 6993–7000. [CrossRef]
31. Tang, W.; Ni, H.; Zhang, Q.; Ding, J. Novel Optical Temperature Sensor Based on Emission in Pr^{3+} Doped Ferroelectric $Ba_{0.7}Sr_{0.3}TiO_3$. *RSC Adv.* **2018**, *8*, 23996–24001. [CrossRef]
32. Li, H.; Pang, R.; Jiang, L.; Li, D.; Zhang, S.; Zhang, H. Exploring the Luminescent Thermometer and Optical Storage Applications in Negative Thermal Quenching Phosphor of $BaSc_2Ge_3O_{10}$:Pr^{3+}. *Ceram. Int.* **2023**, *49*, 32635–32641. [CrossRef]
33. Meng, M.; Wang, P.; Hu, X.; Zhang, M.; Yang, B.; Hua, Y.; Cai, M.; Calvez, L.; Zhang, X.; Xu, S. Exploring Interfacial Reactions and Optical Properties of ZBLAN-Based Phosphor-in-Glass Color Converters via Spark Plasma Sintering for Laser-Driven Lighting. *Ceram. Int.* **2023**, *49*, 28886–28893. [CrossRef]
34. Wang, P.; Lin, H.; Chen, G.; Weng, W.; Xu, Y.; Lin, Y.; Xu, J.; Cheng, Y.; Wang, Y. Rapid Sintering of High-Efficiency Phosphor-in-Glass Films for Laser-Driven Light Source. *Nat. Commun.* **2025**, *16*, 2807. [CrossRef]
35. Aly Taleb, Z.E.A.; Saidi, K.; Dammak, M. High-Precision Optical Thermometry Using Pr^{3+}-Doped $NaCaY(MoO_4)_3$ Luminophores: A Multi-Spectral and Chromaticity-Based Approach to Non-Contact Temperature Sensing. *RSC Adv.* **2025**, *15*, 5327–5337. [CrossRef]
36. Tian, X.; Li, J.; Sheng, H.; Li, T.; Guo, L.; Ji, C.; Huang, Z.; Wen, J.; Liu, X.; Li, C.; et al. Luminescence and Optical Thermometry Based on Silico-Carnotite $Ca_3Y_2Si_3O_{12}$:Pr^{3+} Phosphor. *Ceram. Int.* **2022**, *48*, 3860–3868. [CrossRef]
37. Sharma, S.K. Exploring the Possibility of Using Stark Lines of Pr^{3+} in $CaTiO_3$ Perovskite for Low Temperature Luminescence Thermometry. *J. Phys. Chem. C* **2023**, *127*, 22934–22942. [CrossRef]
38. Bolek, P.; Van Swieten, T.; Zeler, J.; Meijerink, A.; Zych, E. Luminescence Thermometry of Pr^{3+}-Doped $Sr_3Y_2Ge_3O_{12}$ and $Sr_3Sc_2Ge_3O_{12}$ Submicron Garnets Spanning the 13-1025 K Range and New Insight to Their Spectroscopy. *Chem. Mater.* **2024**, *36*, 8894–8909. [CrossRef]

Disclaimer/Publisher's Note: The statements, opinions and data contained in all publications are solely those of the individual author(s) and contributor(s) and not of MDPI and/or the editor(s). MDPI and/or the editor(s) disclaim responsibility for any injury to people or property resulting from any ideas, methods, instructions or products referred to in the content.